RSC Advances

PAPER

View Article Online
View Journal | View Issue

Cite this: *RSC Adv.*, 2016, **6**, 62680

Pt decorated *Artocarpus heterophyllus* seed derived carbon as an anode catalyst for DMFC application†

P. Rupa kasturi,[a] R. Kalai Selvan*[a] and Yun Sung Lee[b]

A carbohydrate rich *Artocarpus heterophyllus* seed (AHS) is processed *via* a hydrothermal carbonization method (HTC) for various reaction times (12, 18, 24 and 30 h) and further thermally carbonized at 700 °C under N_2 atmosphere to sequester a high surface area carbon. Subsequently, Pt NPs are also decorated on the prepared carbon and this was used as an anode catalyst for a methanol oxidation reaction (MOR). The XRD and Raman spectra showed the as-synthesized material has a typical graphitic structure of carbon and an fcc structure of platinum with a grain size smaller than 3–4 nm. The presence of functional groups including –OH, –C=O and –C–O are identified along with some heteroatoms on the surface of carbon through Fourier transform infrared (FT-IR) spectroscopy. X-ray photoelectron spectroscopy analysis exposed the presence of expected species such as C 1s, O 1s, N 1s and Pt 4f. Moreover, BET analysis of the spherical hydrochar carbonized at 700 °C showed a surface area of 431.5 $m^2\ g^{-1}$ with a mean pore diameter of 3.2 nm and a pore volume of 0.354 $cm^3\ g^{-1}$. Morphological analysis such as Field Emission Scanning Electron Microscopy (FE-SEM) and Transmission Electron Microscopy (TEM) images revealed the spherical nature of the obtained hydrochar as well as its transformation into an agglomerated network after carbonization at 700 °C. The obtained Pt loaded carbon showed an excellent electrocatalytic activity in the potential range of interest with a high ECSA of 261.4 $m^2\ g^{-1}$ for Pt/C (hydrochar formed during 24 h and carbonized at 700 °C). Moreover, the Pt decorated optimized carbon sample has much higher peak current and mass activity of about 0.32 mA mg^{-1} and 54.4 A g^{-1} towards MOR. In addition, chronoamperometry analysis also exposed a good stability over 10 000 s. It is also legitimated that a 20 : 80 wt% of Pt/C loading shows a high current density with no relevant change in the onset potential and long-term stability during MOR with a few comparable results.

Received 4th March 2016
Accepted 7th June 2016

DOI: 10.1039/c6ra05833g

www.rsc.org/advances

1. Introduction

Interlinking "life science" as one among the major criteria in engineering an efficient electrocatalyst for energy storage devices like "Fuel cells" is the aim of this work. Man has all kinds of expertise for designing and leading a sophisticated life but still he is scared of the hazardous chemical sources utilized to build such a system. In order to revolutionise, people have started to prefer green resources and technology in parallel for the sake of our future posterity. On considering the phrase "Green technology", another phrase that comes to mind is "biomass". There is an enormous amount of biomass materials on the Earth's crust with incredible features. Earth bestows us with infinite renewable biomass resources, but the question is, how much of it is being utilized properly. Biomass precursors can be artificially charcolized for the rapid sequestration of "carbon" within a couple of hours.[1] Researchers across the world are utilizing these materials in variety of energy storage and conversion applications such as fuel cells, batteries, supercapacitors, *etc.* Among these, fuel cells (FCs) are the best known devices that can convert input chemical energy into electrical energy (occasionally heat) with the help of a catalyst to generate a sustainable electrical power output as far as the input fuel is fed into it, with only pure water and heat as its by-products.[2] Operating temperatures and electrolytes classifies these into different types of FCs.[3a,b] Amid them, DMFC is a special type as they are LTFCs (low temperature fuel cells) that use a polymer membrane as an electrolyte and platinum (Pt) as their electrocatalyst. The cost, easy accessibility, quickly recyclable nature, cheap input fuel, renewability as long as they are supplemented with a green source and the corresponding infrastructure of DMFC technology seem so attractive and innovative compared to all other energy storage devices.

[a]*Solid State Ionics and Energy Devices Laboratory, Department of Physics, Bharathiar University, Coimbatore, Tamil Nadu, India-641 046. E-mail: selvankram@buc.edu.in*
[b]*Faculty of Applied Chemical Engineering, Chonnam National University, Gwangju 500-757, South Korea*

† Electronic supplementary information (ESI) available: Fig. S1 and S2. See DOI: 10.1039/c6ra05833g

Whereas, the pure Pt catalyst is readily toxic due to carbon monoxide (CO) species formed during the methanol oxidation reaction (MOR), that results in a poor electrocatalytic activity. Even though DMFCs are widely used in a variety of applications the "expensive and poisoning nature" of Pt seems to be the two major constraints that deter their practical use. Updates in the field of DMFCs highlighted the inevitability of a perfect anode catalyst material[4] with a good electrocatalytic activity for MOR and minimization of the manufacturing cost. To date there are many researchers investigating the construction of a perfect anode catalyst based on Pt nanoparticles (Nps) such as Pt/C, PtRu, PtCO, PtSn, Pt/graphene, Pt/CNT *etc.*[4] but the issue still remains. Therefore, in order to access a solution and make DMFC into a commercial application, in this work a pure biomass derived high surface area carbon decorated with a minimal loading of Pt catalyst for MOR has been fabricated.

It took hours to pick a natural biomass material which is mainly composed of carbohydrates that contain numerous heteroatoms, based on several reports. In general, AHS is a combination of carbohydrates (38.362%), insoluble polysaccharide (starch grains) and other saccharide derivatives. Although carbohydrates are the main component present, lignocellulosic derivatives also play a vital role in the chemistry of an AH seed. In the HTC process, a slightly acidic AHS powder is mixed with water forming an aqueous solution and is mildly heated (180–205 °C) in closed containers, forming condensed, char-like structures with caramelized liquid as shown in (Fig. 1). Hemicellulose consists of various saccharides like (xylose, mannose, glucose, galactose, *etc.*), it appears as a random, amorphous structure, rich of branches, which are very easy to remove from the main stem and to degrade into volatiles (CO, CO_2, some hydrocarbon, *etc.*) at low temperatures.

The advantages of using hydrochar derived carbon based materials as a support catalyst are as they are light weight, plentiful, cheap, often porous, effective, non-toxic, heat resistant, and as they have a high surface area and a versatile nature. Obviously, carbon[5] as organic matter serves as a basic building block in all living habitats whether it is a flora, fauna, human or a biomass substance. A biomass material is naturally designed with carbohydrates which are composed of three constituents of sugars: monosaccharides, disaccharides and polysaccharides, with three major elements carbon (C), hydrogen (H) and oxygen (O) and a ratio of two H for every single O atom. The precursor material used here is called as "The king of fruits" – *Artocarpus heterophyllus* seed (AHS), and is comprised mainly of polysaccharides, a package of starch along with some lignocellulosic molecules. At large, seeds naturally store carbohydrates in the form of starch (amylose or amylopectin).[6] These seeds are normally discarded or eaten as a snack but here they are used as a precursor material to extract hydrochar by a famous method called "hydrothermal carbonization (HTC)".

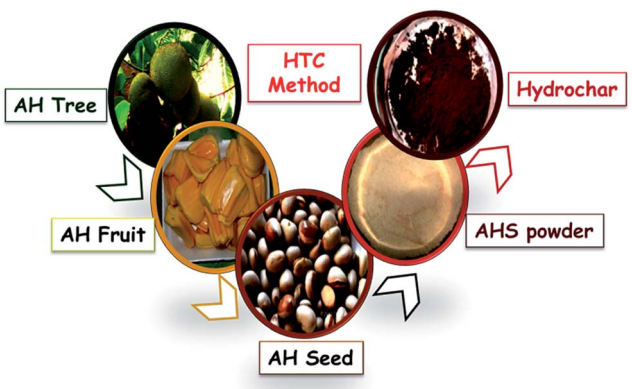

Fig. 1 Preparation of hydrochar *via* HTC method.

Carbon material is sequestered using various synthetic approaches among which hydrothermal carbonization method (HTC) is quite elite. The temperature ranges between 180 °C and 290 °C, the pH of the feed should be below 7, process times varies between 1 and 72 h, and it is a self-contained process without odour (or) noise emissions. Carbon is retained with attractive surface functionalised patterns located on the external surface and highly efficient exothermic process.[7a] HTC was first introduced by Bergius and Specht in 1913, who described the hydrothermal transformation of cellulose into coal-like materials. A HTC process is a homogeneous or heterogeneous chemical reaction in the presence of solvent above room temperature and at >1 atm pressure in a closed autoclave system.[7b] In general, the mechanisms involved in HTC are hydrolysis, dehydration, decarboxylation, condensation, polymerization and aromatization.[8] In a HTC process, the carbon efficiency (CE) is very close to 100%. Almost all the biomass is converted into carbon material, without forming excess CO and CO_2.

Pt decorated carbon is an almost universally known anodic catalyst, which prevents the disadvantages of either a pure Pt (or) a bi-metallic catalyst. Pt decorated carbon catalysts are desirable due to their high surface-to-volume ratios and facile access to each catalyst particle.[9] The catalytic powders used for DMFC are either metal black or supported catalysts on carbon particles at various loadings. Both of these are widely used. At present, the most promising anode materials for DMFCs are carbon supported Pt catalysts.

2. Experimental methods and materials

High pure analytical reagent grade chloroplatinic acid (H_2PtCl_6, Pt-40%) and sodium borohydride ($NaBH_4$) were used for the synthesis and chemical reduction of platinum nanoparticles. Absolute ethanol (CH_3CH_2OH, A.R. grade, >99.7%), methanol (CH_3OH, A.R. grade, >99.5%), sulfuric acid (H_2SO_4, A.R. grade, >99.9%), 20% E-TEK Pt/C, and ultrapure N_2 gas was used for methanol oxidation reaction. All the aqueous solutions were prepared with double-distilled water. All the chemicals were used as received without further purification.

2.1 Hydrochar synthesis

Ripe *Artocarpus heterophyllus* seeds (AHS) were collected from the local market, Pollachi, Tamilnadu, India. The AHS were cleaned and the white arils (seed coats) were peeled off and

blended in a blender to obtain a smooth light brown-pink coloured powder. An amount of 5 g of the resulting mixture was well dispersed in 45 mL of double distilled (DD) water. An acidic catalyst (citric acid) with a concentration of 10 mg was initially dispersed in 5 mL of DD water and then was added to the above mixture in order to enrich the surface morphology of the final mixture. The AHS powder was first hydrothermally carbonized in a Teflon lined autoclave containing 50 mL of water and citric acid at 180 °C for 12, 18, 24 and 30 hours. After being cooled to room temperature, the obtained hydrochar was centrifuged at 5000 rpm for 15 min with DD water and ethanol to isolate the solid brown residue. This was repeated several times to remove all the impurities, and finally this was vacuum dried at 40 °C for 24 h in a programmable oven. The resultant hydrochar samples were further pyrolysed in a tube furnace at 700 °C under constant N_2 atmosphere for 3 h. The obtained carbonized samples were named as C-1, C-2, C-3 and C-4 on the basis of the reaction times of 12 h, 18 h, 24 h and 30 h, respectively.

2.2 Preparation of Pt/C catalysts

In a classic procedure, around 40 mg of each carbon sample was dispersed in 75 mL of DD-water. The mixture was kept under sonication for 30 minutes at room temperature. Subsequently, the mixture was added rapidly to 6.8 mM of H_2PtCl_6 with a pipette and sonicated further for 2 h at an ambient temperature to produce a clear and homogeneous solution.[10,11] After 2 h, an aqueous solution containing 25 mL of 13.6 mM $NaBH_4$ was added dropwise into the solution for chemical reduction of the platinum and this was sonicated for another 2 h. The probable overall reaction mechanism for the above synthesis involves,

$$NaBH_4 + H_2PtCl_6 + 3H_2O \rightarrow Pt + H_3BO_3 + 5HCl + NaCl + 2H_2 \quad (1)$$

Finally, the obtained metallic black coloured solution with foamy appearance was centrifuged at 5000 rpm for 1/4 h with DD-water and ethanol to remove the chloride impurities and finally vacuum dried at 40 °C for 24 h in a programmable oven.[12] The final powder was ground manually with a mortar for 15 min and weighed carefully. The as-obtained Pt decorated samples were denoted Pt/C-1, Pt/C-2, Pt/C-3 and Pt/C-4 respectively.

2.3 Electrode fabrication

The working electrode was fabricated as follows: in case of MOR, 2 mg of the Pt/C catalyst (the ratio of Pt/C composite used was 20 : 80%) and 2 mL of double distilled water was dispersed into a homogeneous black suspension with ultrasonication for 30 min to enhance the uniformity of functionalization.[12] Prior to surface coating, the glassy carbon electrode (GCE) was polished carefully with alumina slurry and rinsed with DD water followed by ultrasonication with acetone and DD water for 15 min. After that, for each electrode, a measured volume (3 μL) of the catalyst solution was cast evenly by a micropipette onto the freshly polished GCE, and dried in vacuum oven at 30 °C for an hour. It is noteworthy that the electrode fabrication of all the samples was carried out in a similar manner.

2.4 Electrochemical measurements

The electrocatalytic activity (Cyclic Voltammetry (CV) and chronoamperometry (CA)) of the Pt/C electrocatalyst for MOR was investigated in a stream of N_2 bubbled through 0.5 M H_2SO_4 solutions containing 1.0 M CH_3OH by applying a potential sweep at a scan rate of 10 mV s^{-1}. Subsequently, the electrochemical investigation was done using a conventional three-electrode system. The electrochemical active surface area (ECSA) and mass activity (M_A) of the catalysts was estimated from the hydrogen electrosorption curve, which was recorded between −0.2 and 1.0 V in a 0.5 M H_2SO_4 solution at a scan rate of 10 mV s^{-1}.

2.5 Instrumentation techniques

The surface morphology of the hydrochar after different reaction times was characterized using scanning electron microscopy (SEM) on a Hitachi S-400 and the distribution of Pt NPs on carbon was perceived by transmission electron microscopy (TEM) and high resolution-TEM (HR-TEM) using a JEOL JSM-2100 microscope with an acceleration voltage of 200 kV. The elemental analyses of the samples were carried out using techniques of energy dispersive X-ray spectroscopy (EDXS). The phase purity and crystallinity of carbon as well as Pt loaded carbon were investigated using powder X-ray diffraction measurement on a Rigaku D/max-2500 with a Cu Kα ($\lambda = 1.54$ Å). X-ray photoelectron spectroscopy (XPS) employed to characterize the binding energy of the surface C, O and N elements was performed on an ESCALAB 250 instrument, and C 1s (284.6 eV) was used as a reference for the binding energy. Raman spectra of the powder samples were recorded on a LabRAM HR Raman microscope with a laser excitation wavelength of 532 nm. The specific area was calculated by the Brunauer–Emmett–Teller (BET) method and the infrared spectra were collected on a vertex 70 Fourier transform infrared (FT-IR) spectrometer (Bruker) to attain information about the functional groups present in the pyrolysed carbon sample. Electrochemical measurements, including the Cyclic Voltammetry (CV) and chronoamperometry (CA) were done with SP-150, Bio-Logic Science instruments, utilizing a conventional three-electrode cell at room temperature. 0.5 M H_2SO_4 and 1.0 M CH_3OH were employed as electrolytes. The counter electrode was a platinum wire (0.5 mm in diameter and 30 cm in length), and the reference electrode was an Ag/AgCl. The catalyst was dispersed on the glassy carbon (GCE) electrode (3 mm in diameter) and used as the working electrode.

This work revolves around four major synthesis sections consisting of the hydrochar preparation *via* low temperature HTC (hydrothermal carbonization) at various reaction times, carbonization of the hydrochar at high temperatures, Pt reduction by a standard chemical reduction method and finally the reduced Pt NPs will be decorated on the carbon to fabricate a Pt–C (Pt decorated on carbon) electrocatalyst. The designed

electrocatalyst can then be used as an anode catalyst in a Direct Methanol Fuel Cell (DMFC).[10,12]

3. Results and discussion

3.1 Physico-chemical characterization of hydrochar

To check the physical purity, presence of functional groups, intelligibility, and finally the morphology of the samples during hydrochar formation they were subjected to XRD, FT-IR, Raman and FE-SEM analysis as shown in Fig. 2a–f. The samples initially underwent X-ray scattering and exhibited a wide diffraction peak at $2\theta = 10°$ to 30° (002-vertical plane position) due to the epoxies, carboxyl and hydroxyl groups prevailing in the hydrochar samples. Moreover, these functional groups are responsible for their hydrophilic nature and confirms that the AHS belongs to type A starch.[13,14] In addition, XRD clearly reveals that the peak belongs to an amorphous state of carbon called a turbostratic structure (half boiled state) with more aromatic features (coffee type fragrance). The surface of the hydrochar seems to be turbostratic as the starch gelatinization process occurred in the presence of water molecules along with a mild breakage of lignocellulosic derivatives during the low temperature hydrothermal carbonization process. Starch and saccharides[15] are forms of carbohydrates stored in plants and are the main components of AHS powder. Henceforth, during HTC process at 180 °C, starchy polysaccharides and lignocellulosic derivatives endure a set of thermal phenomena and finally get carbonized into microspheres.[16]

The FE-SEM images show a very clear difference among the hydrochar samples carbonized for different reaction times 12 h (HTC-12), 18 h (HTC-18), 24 h (HTC-24) at 180 °C. Rupturing and textural changes occurred in the lignocellulosic structure in response to the hydrothermal carbonization (HTC) process. It can be seen that the majority of the starchy networks retained their properties even after 12 h of reaction time with the image showing patchy fibrous linkages, while at 18 h the fibrous network had broken down completely to build dumbbell shaped grains everywhere. This situation implies the importance of reaction time and how it influences the particle size. Magnificently, after 24 h the starchy networks vanished completely while the dumbbell grains fragmented into smooth surfaced carbon with spherical shape morphology. The formed spheres had a diameter of about 10 μm.

The reaction happening inside the autoclave at temperatures above 170 °C at various reaction times, essentially fixes the entire C, and thus generates a colloidal brown mixture, which is named hydrochar (hydrothermal reaction and carbon). This hydrochar material is usually packed with clustered polar functional groups such as carboxylic, hydroxyl and oxygen, along with some heteroatoms being anchored to its surface top.[17] The presence of surface moieties may enhance the catalytic property of the material. With this morphological view, the hydrochar was further scrutinized by means of FT-IR. It was presumed this was out the presence of functional groups and the water content affixed to the surface of the carbon. This exposes its importance on the sequestration ability of the material. Moreover, the formation of organic compounds

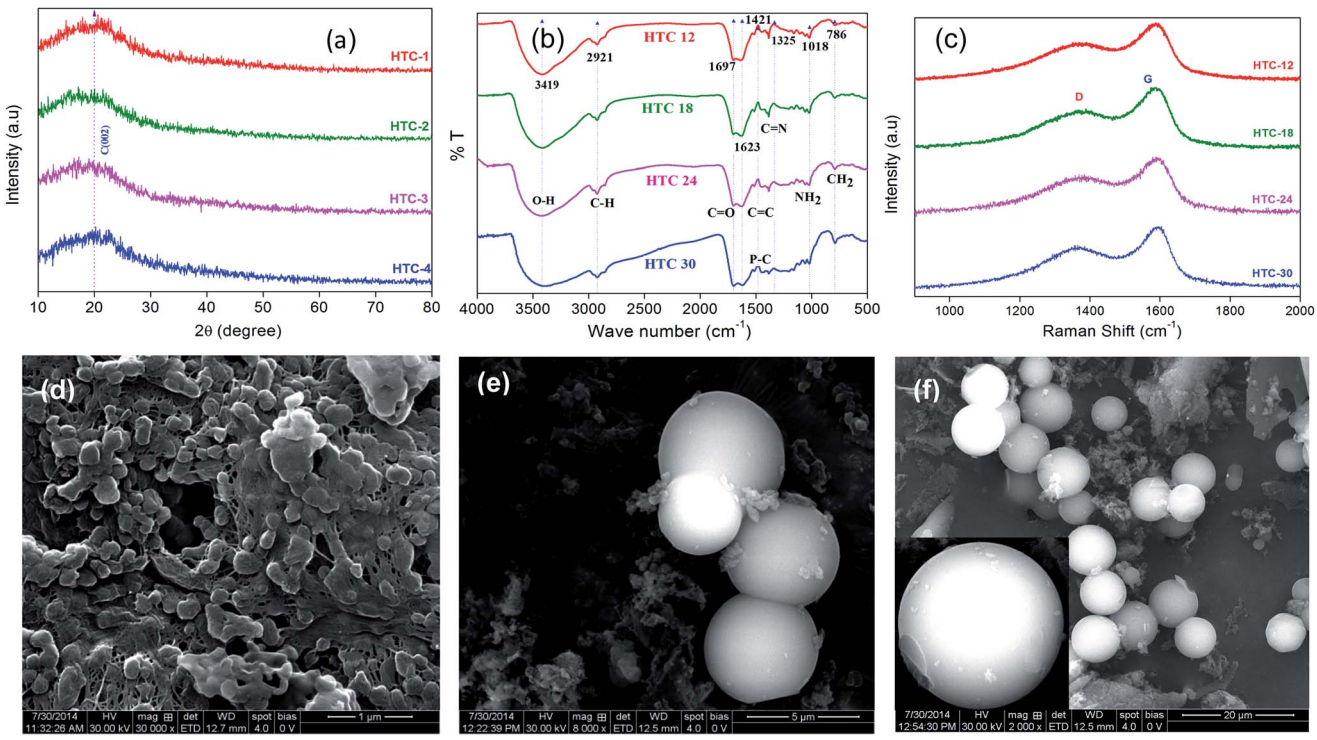

Fig. 2 (a) XRD, (b) FT-IR (c) Raman and FE-SEM images (d) 12 h (patchy network), (e) 18 h (dumbbell shape), and (f) 24 h (spherical shape) of hydrochar samples autoclaved at 180 °C.

during HTC is the key responsible factor for the formation of bands in the FT-IR spectra.

The band assignments for the spectra of AHS contain a number atomic groups and structures (O–H, C–H, C=O, CH_2, C–O, N-containing bioligands and so on). The broadened and intense bands ranging from 3400 cm^{-1} to 3500 cm^{-1} are assigned to the involvement of O–H groups (adsorbed water molecules on the surface), indicating the presence of phenols and alcohols. The stretching of O–H bond vibrations within this range of frequency indicates the presence of O–H bonds of carboxylic acids or free hydroxyl groups present in the hydrochar.[18] Besides this, the added citric acid on the biochar enhances the acidic environment (pH = 5) which helps hydrogen bond breakage; as a result the hemicellulosic grid attached to the hydrochar becomes degraded. A clear band in the range 2900 cm^{-1} to 2800 cm^{-1} indicates CH_2 symmetric (or) CH_3 asymmetric stretching vibrations of aliphatic C–H and O–H acids (hydroxyl or carboxyl), respectively. The occurrence of the C–H stretching in aliphatic groups is due to methyl, methylene and methane groups bonded to aromatic carbon. Phenols and carbonyls[19] are less acidic while carboxyl groups (COOH) are strong. The C–H group present in the hydrochar is one among the main reason for the formation of spherical shape carbon with smooth surface as signified by FE-SEM image.

Ether linkages in hemicelluloses were affirmed by the bands emerging at 1680–1740 cm^{-1} due to C=O stretching of the esters, aldehydes and carboxylic groups (C_6H_5–C=O), while those at 1500–1623 cm^{-1} correspond to C=C groups (alkenes), which reveals the truth behind the process of aromatization and furan ring opening in the hydrochar material during polymerization and it correlates the (G band) E_{2g} mode of highly oriented pyrolytic graphite (as mentioned in Raman analysis), and hence reveals the complete aromatization of the samples.[20a,b] This suggests that the carbon spheres are composed of more crystalline graphitic carbon due to which they are indicated to be turbostratic (concordantly with XRD) and the higher intensity of the G-band is due to the higher degree of graphitization with fewer defects. The presence of secondary amides, N–H bending along with C–N vibrations are confirmed by a band at 1510–1540 cm^{-1}, is caused by protein molecules. A band around 1325–1350 cm^{-1} was caused due to the presence of an aromatic nitro compound NO_2 stretching, while that at 1320–1336 cm^{-1} was due to CH_2 wagging and 1365–1382 cm^{-1} due to C–H bending. Some broad bands seen around 830–1019 cm^{-1} correspond to NH_2 amine groups. An IR band found around 780–800 cm^{-1} was assigned to the aromatic C–H out-of-plane bending vibration. Bands expressing these groups indicate that there are many –OH, –C=O and –C_6H_5–C=O groups left on the surface of the hydrochar. Likewise, that at 480–800 cm^{-1} indicates the presence of N-containing bioligands.[21] The occurrence of numerous bands on the surface top is the result of hydrolysis, dehydration, condensation and aromatization occurring during the HTC process. Subsequently, in order to survey the elemental occurrence in the hydrochar, EDX analysis was employed, (Fig. S1, ESI†) and clearly indicates the presence of the expected excess carbon (C) of about 93%. Beside C, spectra also comprise signals with heteroatoms like nitrogen (N-7.4%) and sulphur (S-0.05%). The presence of N and S elements in the material[22] is a bonus, as they enhance the electrochemical behaviour of the material. Areas of high N are centres of high basicity. The other minor functional groups found to be naturally occurring in the prepared hydrochar were sulphonates and sulphates.

Apart from the elemental study, the Raman spectra of all the four hydrochar samples show very low intensity D bands at 1370 cm^{-1}, activated by the presence of disorder in the carbon systems, and a sharp G band at 1592 cm^{-1} that corresponds to the tangential vibrations of the graphite carbons (*i.e.* turbostraticity), which is consistent with the XRD results. The graphitization degree of all the samples measured using the intensity ratio (I_D/I_G) is around 0.86 with a domain size of about 51.16 Å. Irrefutably, all the studies explored the evolution of turbostratic microsphere shaped carbon incorporated with enormous functional groups[23] on their surfaces with less disorder, which emerged as a product of the HTC method with no palpable change in the property of the AHS derived hydrochar prepared at diverse reaction times except in case of the morphological factor.

The reason for the above mentioned structures such as fibrous, dumbbell and the evolution of a spherical shape structure during HTC is due to the united reactive behaviour of starch polymer molecules under such a temperature, the moieties become aggregated into one immense molecule with a 3-d structure that fills the liquid at >170 °C. As we know AHS contains complex carbohydrates which undergo various chemical pathways[24] during HTC such as hydrolysis, dehydration, formation of carbonyl, carboxyl, and hydroxyl groups (condensation) (in concordance with the FT-IR analysis) and aromatization (sphere formation). At an elevated temperature the dampness of the sample in the autoclave expedites a major surface reaction: the hydrolysis reaction of organic products. A hydrolysis process directly influences the starchy carbohydrate (polysaccharides – bio-macromolecules) linkage by breaking their ether bonds (C–O–C) and forming simpler carbohydrate molecules like disaccharides (sucrose, maltose and lactose) in the presence of an acidic catalyst. By increasing the reaction time, these oligomers disintegrate into their corresponding monosaccharides (glucose, fructose and galactose) attached with O, C, H and OH groups. These monomers[25,26] undergo dehydration by losing three water molecules to form furfural or 5-hydroxymethyl-furfural (HMF) like products,[27] which are probably a responsible factor for the particle size and the presence of alcohol and aldehyde groups observed in the FT-IR spectra.In general, a medium composed with furans and dehydrated saccharides is highly favourable for the formation of carbon. Also, dehydration plays a vital role for the formation of functional groups on the surface. During HTC, the monomers (glucose) degrade to form a HMF intermediate, which finally condenses into a carbon-like material. The generated HMF is a yellowish water soluble monomer comprised of aldehyde and alcohol functional groups. Due to the acidic nature of the medium, HMF dehydrates to form a caramelized liquid and an extended polyfuran-type aromatic cluster through polymerisation. Subsequently, when the concentration of these

aromatic clusters[28] reaches a critical supersaturation point due to reaction time, a burst nucleation takes place. The nuclei thus formed, burst outside by diffusion forming microspheres[28] containing an sp^2 hybridized backbone (also responsible for the brown colour) decorated with numerous polar oxygen functionalities (–OH, –C=O, –COOH *etc.*) present both on the outer surface as well as in the reactive species. Moreover, pH plays a key role here; the strong acidicity may prohibit oxygen functionalities from diffusing and linking to the nuclei[29] and stops the growth of carbon microspheres. This whole reaction process forms a C–C bond break and furan ring opening[30] as seen in the FT-IR data. Likewise, the C–H bond in FT-IR spectra are owed to the formation of different fural-like compounds, which decompose inside the autoclave to form phenols, acids and aldehyde groups, this leads to the formation of soluble polymers due to an intermolecular polymerization[31] reaction. Thus, the overall mechanism for the formation of these functional groups during the HTC process is that a set of dehydration reactions leads to carbohydrates forming HMF/furfural derivatives while polymerization towards polyfurans, aromatization and nucleation bursts ends with the creation of a smooth spherically structured hydrochar according to the LaMer model,[31] which is a combination of condensed furan rings bridged by aliphatic, hydroxyl and carbonyl functional groups. Hence, incompletely developed microspheres were formed. Samples treated at 180 °C showed only poor or no methanol oxidation reactions regarding the electrochemistry (shown in Fig. S2, ESI†). Hence, the current work was taken to the next level by the activation of the hydrochar samples at a higher carbonization temperature of 700 °C in the presence of pure N_2 gas. Hydrochar samples treated in such a high temperature undergo series of interrelated physical and chemical changes. The physical characteristic changes during pyrolysis include strength, colour and crystallinity. These physicochemical and structural changes were examined through a variety of analytical techniques and compared with the above empirical results before beginning a MOR mechanism. These empirical results indicate how the varying reaction times influence the morphological features during the HTC synthesis of hydrochar despite the fact that all samples almost have the same crystal structure, particle size and functional groups (higher oxygen and hydrogen).

3.2 Physico-chemical characterizations of carbonized hydrochar

The phase purity and crystallinity of the samples were examined using X-ray diffraction analysis. Fig. 3 shows the XRD pattern of hydrochar prepared after various reaction times (C-1 (12 h), C-2 (18 h), C-3 (24 h) and C-4 (30 h)) carbonised at 700 °C under N_2 atmosphere as shown in (Fig. 3a). The carbonized samples exhibit a broad peak at $2\theta = 24.5°$ which corresponds to the (002) plane.

The broadening of the peaks is due to the presence of epoxies, carboxyl and hydroxyl groups between the carbon atoms, which makes it hydrophilic[32] and brown. In addition, a peak found at $2\theta = 43.5°$ corresponds to the (100) vertical

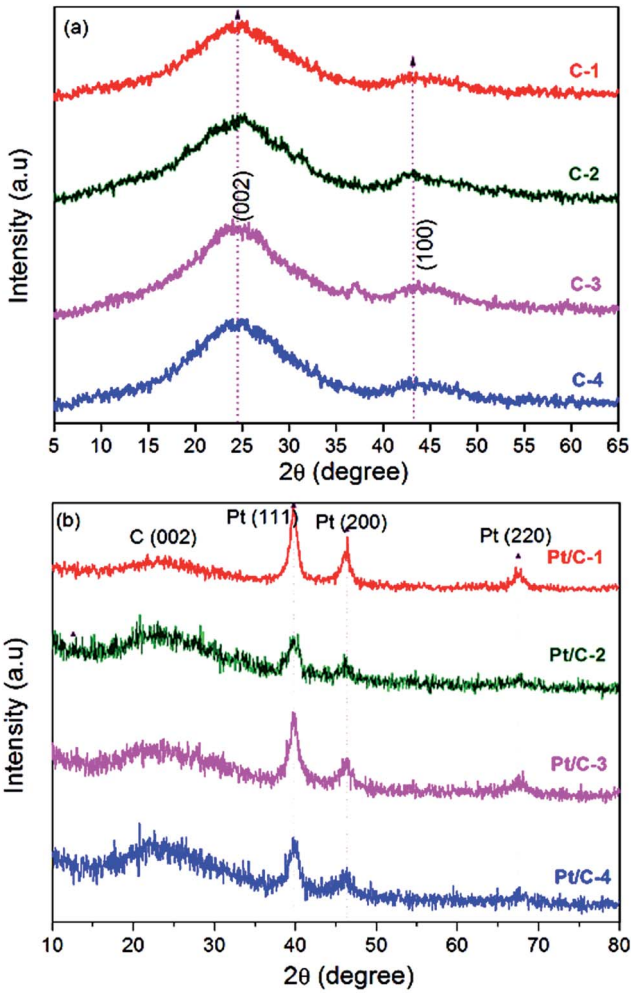

Fig. 3 XRD patterns of (a) hydrochar samples carbonized at 700 °C with N_2 flow and (b) Pt decorated carbon catalysts.

plane. These peaks indicate that the obtained carbon is composed of a graphitic structure. The turbostraticity of hydrochar may be due to the char formation and caramelization of polysaccharides that occurred during HTC. It can be seen that the intensity of the graphitic carbon peak (graphitization) increases after carbonization ($2\theta = 24.5°$) compared to the hydrothermally carbonized AHS samples. The reason for such amorphous nature of AHS was due to partial crystallinity of the granules belonging to type-A starch,[32] which has a structure of open cylindrical pores at both ends and so there is less space for water molecules. Furthermore, Fig. 3b shows the XRD patterns of the platinum loaded carbon composites. A fairly wide X-ray (002) peak detected at a 2θ value of 23.5° is due to the presence of carbon. In addition, the three strong diffraction peaks observed at Bragg angles of 39.7°, 46.1° and 68.0° which can be dispensed to reflections from the (111), (200) and (220) planes of face centered cubic Pt, indicating a good crystallinity and confirming that the Pt NPs are properly reduced and decorated on the carbon surface.[33a] Subsequently, the broadness of the peaks reveal that Pt NPs are small in crystalline size. The crystalline size (D) of the Pt NPs and the surface area of the Pt/C

catalyst were determined with respect to the Pt(111) reflection plane using the Scherrer equation,

$$D = \frac{K\lambda}{\beta \cos(\theta)} \quad (2)$$

$$S = \frac{6000}{\rho d} \quad (3)$$

where, 'λ' is the wavelength of the X-ray radiation, 1.54 Å, 'θ' is the Bragg angle of the Pt(111) peak diffraction angle, D is the grain sizes (nm), K is the coefficient taken as 0.9, β is the full width at half-maximum height (θ), S is the specific surface area ($m^2\ g^{-1}$), d(111) is the line spacing and ρ is the Pt density (g cm^{-3}). The calculated crystallite size and specific surface area are given in Table 1. This clearly evidences that among the prepared samples, the Pt/C-3 has low crystallite size (2.7 nm) and high specific surface area (103.8 $m^2\ g^{-1}$) which may improve the electrocatalytic behaviour[33b] of the sample.

FT-IR analysis was carried out to understand the nature of the functional groups present in the samples. Fig. 4 shows the FT-IR spectra of C-1, C-2, C-3 and C-4 after carbonization at 700 °C under N_2 atmosphere. The presence of functional groups determines the quality and quantity of chemisorptions of metals onto the carbon surface. It can be observed that the prepared samples lost some of their functional groups when the carbonization temperature reached 700 °C. From a chemical compositional perspective, the prepared AHS hydrochar is encapsulated by oxygen functionalities and hetero-atoms like N and S.[34] These hetero-atoms are bonded to the edges of the carbon layers that govern the surface chemistry of the hydrochar. During carbonization at 700 °C, these elements, C, H, and O, volatilize and cause dehydration and pyrolysis,[34] where H and O are vanished in greater amounts than C.

A broadened region around 3400 cm^{-1} to 3500 cm^{-1} is assigned to hydroxyl groups or adsorbed water motifs. It can be seen that the peak at 3414 cm^{-1} loses its strength when compared to the hydrochar, which is due to the dehydration reactions which happen after carbonization is increased (turbostraticity to graphitic nature). A very weak indication of a C–H group for the sample C-4 at 2925 cm^{-1} is due to the methyl group but this is not present in the other three samples as the carbonization temperature increases.

Carbonyl vibration (C=O stretching) from a saturated aldehyde is found at 1740 cm^{-1}. Bands around 1411 and 1560 cm^{-1} could be due to the complete distortion of water molecules from the hydrochar. The band at 905 cm^{-1} was ascribed to O–H bending vibrations, which suggests an abundance of oxygenated groups in the samples. The overall changes in the position

Table 1 Crystallite size and specific surface area of Pt/C samples

Sample	d(111) nm	Average crystallite size (D) nm	Surface area (S) $m^2\ g^{-1}$
Pt/C-1	0.226	4.7	68
Pt/C-2	0.227	4.4	64
Pt/C-3	0.226	2.7	103
Pt/C-4	0.224	3.0	93.45

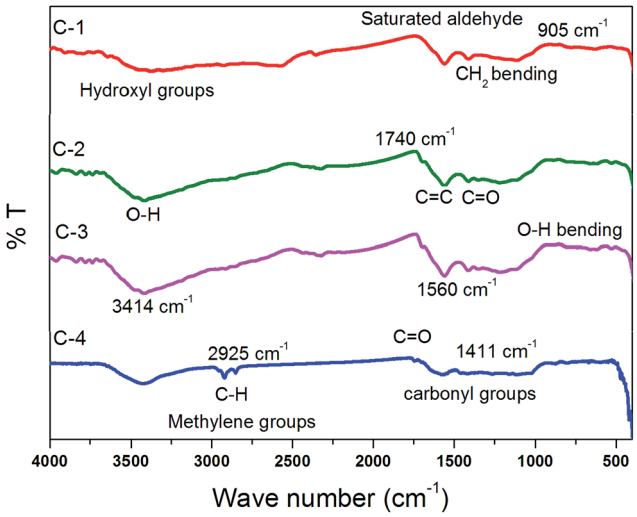

Fig. 4 FT-IR spectra of carbonized hydrochar samples at 700 °C with constant N_2 flow.

and intensity of all the aromatic bands decreases for the carbon prepared at 700 °C, indicating formation of a graphite-like structure and the evolution of volatile products. The presence of more oxygen containing functionalities[35] enhances the electrocatalytic activity by imparting high hydrophilicity to the electrode which favours strong interaction of the aqueous electrolyte ions with the polar groups in the carbon material. The influence of organic groups[36] such as H and N, on the electrochemical performance may be important but it is difficult to explain their role in the electrochemical studies.

XPS surface analyses as shown in Fig. 5 were also investigated for the prepared Pt/C electrocatalysts in order to confirm the elemental occurrence (with their corresponding oxidation states) and their relative intensities. The above XPS multiplex scans obtained data mainly about three major species C 1s, O

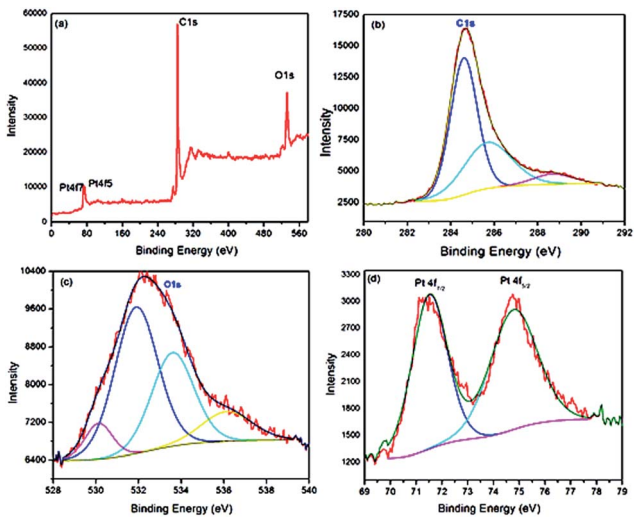

Fig. 5 XPS images of the Pt NP decorated carbon electrocatalysts synthesized at 700 °C, Pt/C-3, (a) survey scan, and (b) C 1s, (c) O 1s and (d) Pt 4f regions.

1s, Pt 4f and their respective peaks.[37,38] The catalyst analyses were split into two intensive doublets as Pt $4f_{7/2}$ and Pt $4f_{5/2}$ with binding energies of 71.06 eV and 74.85 eV as shown in Fig. 5d. The peak arising at the lower binding energy 71.06 eV is indisputably due to a pure metallic (Pt^0) state of platinum with a small cluster size, while a less intensive the peak at the higher binding energy of 74.85 eV is because of Pt(IV) species such as PtO_2 or Pt $(OH)_4$. These oxides may be due to the platinum combining with the oxygen functional groups on the surface of the carbon support. It is concluded therefore, that more than 90% of H_2PtCl_6 was reduced to elemental platinum during the chemical reduction.

Thus, Fig. 5b shows the spectra for C 1s, Gaussian decomposition results in three kinds of bonds with chemical environments. Respectively, carbon atoms in graphitic C–C/C=C (284.6 eV) aliphatic/aromatic carbon groups, C–O like (285.6 eV) carbon atoms, and high valence carbonyl group C=O states (288.6 eV) were observed; oxidized forms of carbon. The C 1s signal could be deconvoluted into carbon peaks in two kinds of chemical environments, the graphitic carbon at 284.6 eV and the C–O or C=O species at 286.3 eV, which is due to the oxidized carbon species[39,40] at the surface.

A high intensity of oxygen was detected on Pt/C due to adsorbed oxygen species as shown in Fig. 5c. The XPS for O 1s is deconvoluted into four major components, 531.89 eV, 533.6 eV, 530.13 eV and 536.13 eV, (530.13–531.89 eV) which are associated with C=O like species and the other binding energies between 533.6–536.13 eV can be assigned to other oxygen[41] containing surface functional groups. The XPS results point out the high concentration of oxygenated groups on the surface of the microparticles in concordance with the FT-IR results.[42] The existence of more oxygen containing functional groups on the surface of the carbonaceous microparticles may be due to the decomposition of hydrochar derivatives during high temperature calcination.

Three peaks assignable to C 1s, N 1s and O 1s indicate the high purity of carbon without the presence of any undesirable compositions. A remarkably low N 1s peak obtained at 400 eV may be attributed to "pyrrolic"-N (N in a five membered ring), which enhances the wettability during MOR, and is the most stable nitrogen species[43] under pyrolysis conditions. It is clear that the nitrogen is present in the hydrochar and forms a strong attachment with the sample even at very high temperatures.[44] The heteroatoms and functional groups present in a carbon matrix can significantly alter the electron/donor characteristics of the carbon electrode material. In particular, the material indeed contains nitrogen, which acts as an electron donor in the lattice, resulting in a shift of the Fermi level in the carbon electrodes.[45,46] As a result, nitrogen atoms doped on the sample enhance the wettability of the interface between the electrolyte and electrodes. Only a very low intensity of N 1s heteroatom is observed, since at high temperatures the carbon surface undergoes surface reconstruction to increase its graphitic nature. Moreover, the increase in the degree of graphitization at higher temperatures was supported by Raman and XRD analyses. In addition, O_2 molecules are more reactive than nitrogen, thus oxygen was more predominant than N at high temperatures.

N_2 adsorption and desorption analysis were carried out to further illustrate the specific surface area and porous nature of the prepared carbon as shown in Fig. 6. Hysteresis between the adsorption and desorption[46] curves reveals the porous nature of the sample. The shape of the isotherm represents type I (Langmuir type) and IV according to the IUPAC classification that it depicts two kinds of hysteresis uptakes in the relative pressure $\rho/\rho_0 < 0.2$ and $\rho/\rho_0 > 0.9$, which exhibits the typical mesoporous (2–50 nm) and slightly macroporous (>50 nm) nature of the sample. Accordingly, the BET surface area (S_{BET}) of the C-3 is about 431.5 $m^2\ g^{-1}$. Thus, the carbonization of hydrochar at high temperatures seems to be effective in producing highly porous carbon material with a mean pore diameter of 3.2 nm and a pore volume of 0.354 $cm^3\ g^{-1}$ as determined *via* the Barrett Joyner Halenda (BJH) method from the adsorption branch of the nitrogen isotherms. The presence of such an extensive range of macropore and mesopore distributions[47] permits efficient transportation and permeability[48] of methanol through the electrode materials during MOR.

Typical TEM images of the platinum (Pt) NPs supported on AHS derived carbon electrocatalysts synthesized at 700 °C are shown in Fig. 7. The TEM images could clearly expose the particle size as well as how homogeneously the crystalline metallic platinum nanoparticles (NPs) are decorated on the surface of the prepared graphitic carbon. The Pt grains[49] are

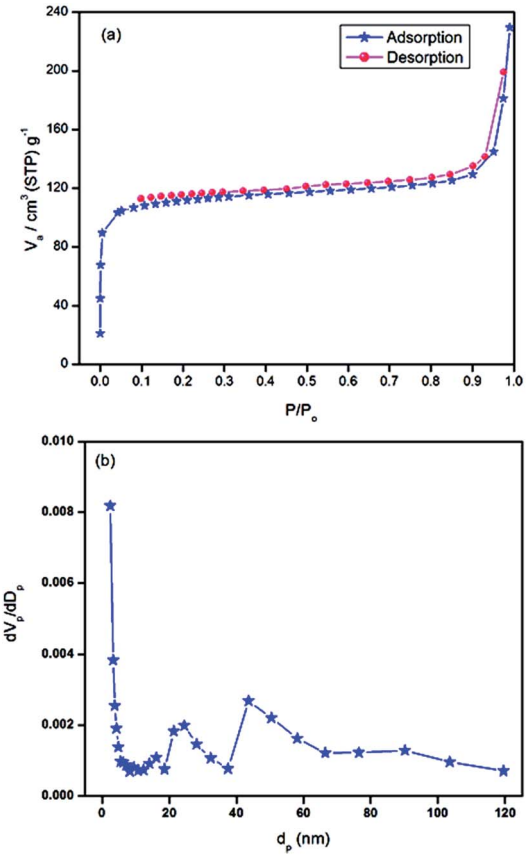

Fig. 6 The (a) N_2 adsorption–desorption isotherms and (b) pore size distribution of C-3 carbonized at 700 °C.

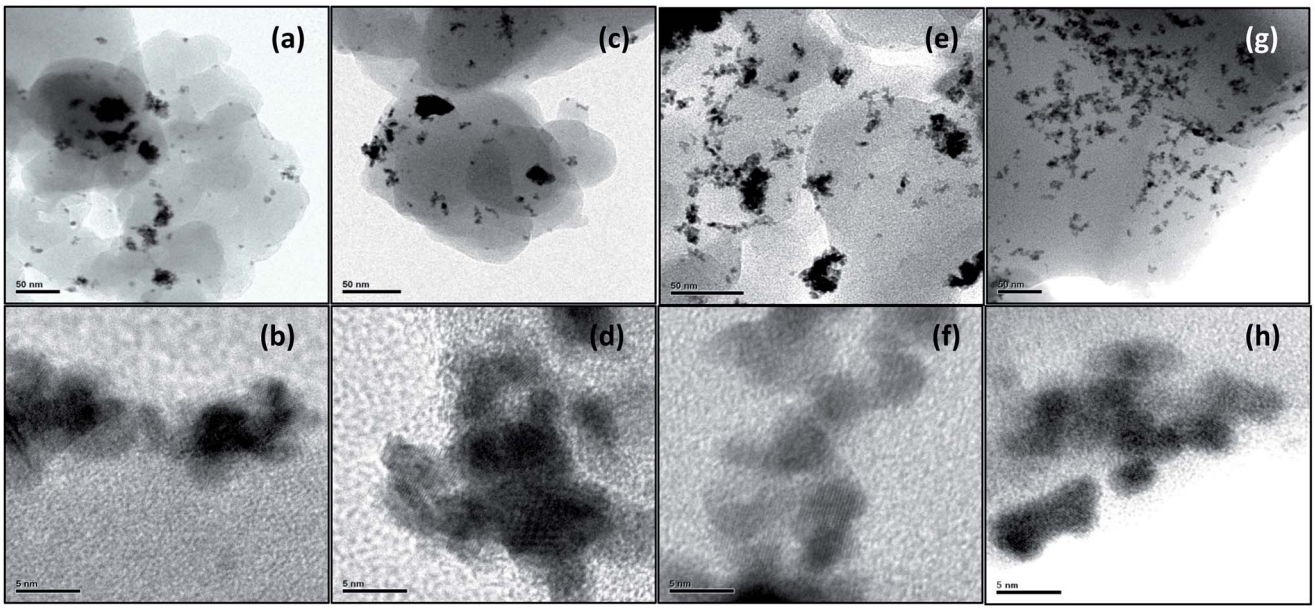

Fig. 7 TEM and HR-TEM images of the Pt NP decorated carbon electrocatalysts synthesized at 700 °C; Pt/C-1 (a and b), Pt/C-2 (c and d), Pt/C-3 (e and f) and Pt/C-4 (g and h).

metallic black while the majority of the carbon supports are grey.

It can be seen that the carbonization process has a direct impact on the physical nature of the hydrochar, where the crystallites become large and tend to agglomerate with one another. Moreover, carbonaceous residue forms and is obtained when hydrochar is thermally degraded under high temperatures. Four stages of changes occur during the calcination process; dehydration, pyrolysis, graphene nucleation[50] and carbonization. From a compositional point of view, the major constituents of the hydrochar (C, N, and S) volatilize during dehydration and pyrolysis, with H and O being completely lost while N is firmly anchored on the carbonized black residue as a heteroatom (XPS). The proportion of C in the solid phase increases after carbonization. This shows the stability of N present in the sample. The whole transformation of functional groups[51] can be clearly seen by representation of FT-IR before and after carbonization. Due to a high contrast between Pt and C, these images mainly reveal the Pt clusters, which appear as black domains. It is noteworthy that the diffraction from Pt metal did not appear as clear spots with definite shape in case of the catalysts Pt/C-1, Pt/C-2 and Pt/C-4, but as tiny black balls with irregular shape morphology, that cover the carbon support with random non-uniform spots as shown in the HR-TEM spectra (Fig. 7). One of the main reasons for the formation of such heterogeneous as well as homogeneous platinum crystallites on the same platform is due the chemical reduction of H_2PtCl_6 *via* a $NaBH_4$ reduction route. Exceptionally, in the case of Pt/C-3, it is quite obvious to see both the Pt NPs and carbon support have regular sphere shaped morphological bridge visible as shown in Fig. 7e, although the metallic particles form an aggregated network in some nooks, these were well dispersed on the surface top of each grain belonging to the carbon support. Moreover, an advantageous factor of the Pt NPs and the carbon motif is that the water media used won't affect the Pt/C catalysts at any point.

Moreover, the clear lattice fringes observed on the HR-TEM image enables one to calculate the *d*-spacing and the particle size of Pt NPs, especially the platinum NPs belonging to Pt/C-3 electrocatalyst which show a very well defined sphere shaped crystal structure with *d*-spacing 2.31 Å for the atomic plane Pt(111) and has an average size in the range of >5 nm, which well matches with the XRD analysis spectrum of Pt (NPs), which implies that the Pt particles are mostly single-crystalline with fcc structure. The average size of the Pt particles decorated on the graphitic carbon are obtained directly by measuring the sizes of 15–20 particles randomly, that are in the range 3–4 nm. Also, the broad and sharp peaks that appeared in the XRD pattern are due to the impact of particle size of Pt NPs.[52]

Significantly, these tiny Pt NPs decorated on the carbon surfaces can act as "spacers" to prevent aggregation and restacking, so both the faces of carbon are accessible. Such aggregation of Pt NPs is found on each carbon sphere due to the presence of localized defects and facilitates the high dispersion and immobilization of Pt particles which makes the carbon surface chemically active for the enhanced interaction with Pt and supports the ionic conductivity during MOR.[53] No free particles are observed in the background of the TEM images which confirms the results of platinum loaded XRD. Also the sizes of the Pt NPs are drastically smaller than the diameter of carbon spheres. It is not conclusive whether they are outside or inside the spherical carbon, but the assumption is that they are only coated on the surface top. Therefore, the resultant Pt/C-3 nanocomposites can be declared to have great potential as an electrocatalyst for DMFC.

3.3 Electrochemical properties

To substantiate our ideology, the prepared platinum decorated carbon samples underwent electrochemical analysis *via* depositing them onto glassy carbon electrodes.[54a,b] Fig. 8 shows the CVs of the Pt decorated on carbon based electrocatalyst (Pt/C-1, Pt/C-2, Pt/C-3 and Pt/C-4) prepared at various reaction times and carbonized at 700 °C by a scan rate of 10 mV s^{-1}. The samples initially underwent potential cycling in 0.5 M H_2SO_4 (Fig. 8a) electrolyte solution at room temperature followed by methanol oxidation reaction (MOR) as shown in Fig. 8b which confirms the typical behaviour of the monometallic Pt/C catalyst.[55]

One of the efficient parameters for determining the catalytic activity of the prepared electrocatalyst is the electrochemical surface area (ECSA) of Pt NPs, especially for MOR. In fact, Fig. 8a shows the CV curve of the electrocatalyst immersed in 0.5 M H_2SO_4 electrolyte solution in the potential range of −0.2 to 1.0 V *vs.* Ag/AgCl with a platinum loading of 0.0571 gm^{-2}. The electrolyte was first de-aerated with N_2 before the ECSA analysis[56] at a scanning rate of 10 mV s^{-1}. The onset potential of hydrogen desorption starts to occur at −0.2 V *vs.* Ag/AgCl and a peak instigated at −0.06 V was followed by an increase in current rate as the negative potential gets higher. This slight peak of the CV is associated with the reduction of H^+ ions and the adsorbed H atoms. During the reverse scan a pair of broad redox peaks were observed between 0.4 V and 0.5 V, this may correlate with the redox behaviour of the carboxylic acid groups (such as –COOH adsorption and –OH adsorption), and as the adsorbed H is desorbed[57] resulting in the generation of anodic current. The magnitude of the current depends on the concentration of the surface groups present in the carbon. Additionally, integration of the charge passed for hydrogen desorption gives (Q_H), the ECSA values for all the electrocatalysts were obtained by the following equation and are provided in Table 2,

$$\mathrm{ECSA} = \frac{Q_H}{0.21 \times L_{Pt}} \quad (4)$$

where, L_{Pt} is the platinum loading (gm^{-2}) on the GCE and 0.21 represents the charge required for the oxidization of a monolayer of H_2 on the Pt particles. Moreover, the electrocatalytic activities for all the catalysts are evaluated using mass specific activity (M_A) with respect to the peak potential for MOR. The M_A was calculated by integration of the charge density[58] corresponding to methanol oxidation divided by metal loading according to the following equation and the values are given in Table 2,

$$M_A = \frac{Q_H}{L_{Pt}} \quad (5)$$

Q is the charge density for the methanol oxidation peak (mC cm^{-2}) and L is the loading of Pt in the electrode (mg cm^{-2}). Subsequently, using the charge passed for H-desorption Q_H, one can estimate the surface area of Pt, S_{Pt}.

$$S_{Pt} = \frac{Q_H}{210} \quad (6)$$

The ECSA, M_A, S_{Pt} values of Pt/C-3 as shown in Table 2 are much higher than those of all the other catalysts which means that the sample Pt/C-3 has a homogeneous dispersion and smaller size of Pt nanoparticles (exact match with GCE, not too large or small) with larger surface area. When Pt/C catalysts are subjected to 0.5 M H_2SO_4, hydrogen adsorption and desorption mainly occurs on the Pt atoms, and the high value of ECSA means that it exposes the maximum amount of Pt atoms on the surface of the carbon.[59] These values show that the catalyst provides a large surface area available for charge and also access

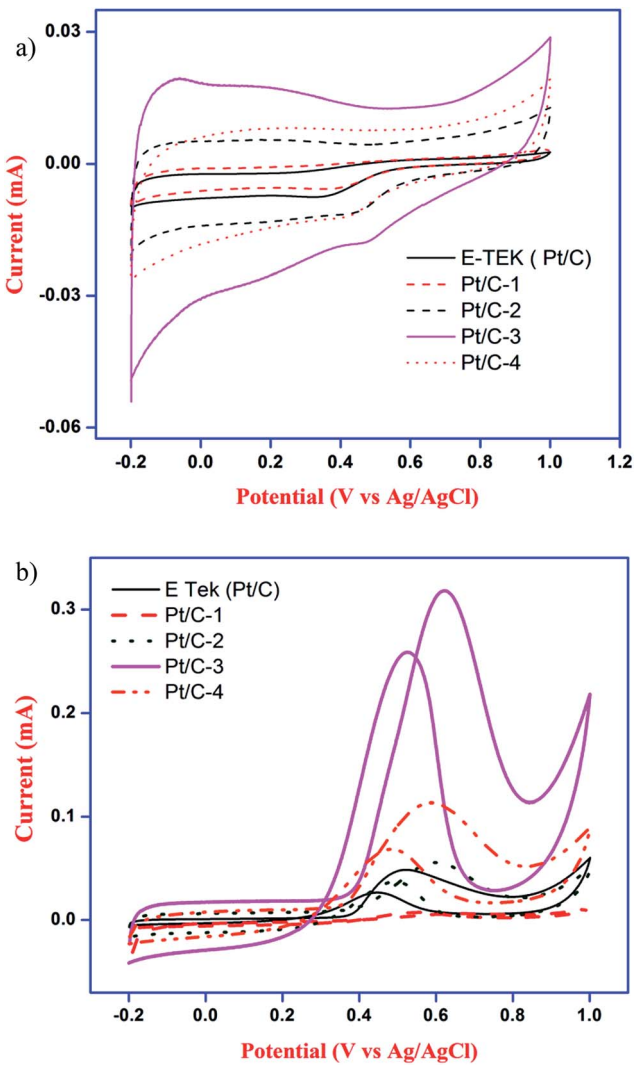

Fig. 8 CV curves of the fabricated Pt/C catalyst in (a) 0.5 M H_2SO_4, (b) 0.5 M H_2SO_4 + 1 M CH_3OH.

Table 2 Calculated ECSA, M_A and S_{Pt} values of Pt/C samples

Sample	ECSA (m^2 g^{-1})	M_A (A g^{-1})	S_{Pt} (cm^2)
E-TEK	136.5	28.44	7.7×10^{-3}
Pt/C-1	124.7	25.98	7.0×10^{-3}
Pt/C-2	58.82	12.26	3.3×10^{-3}
Pt/C-3	261.4	54.4	1.4×10^{-2}
Pt/C-4	68.33	14.2	3.8×10^{-3}

to a conductive path to transfer electrons to and from the electrode surface. Thus the increased current density during MOR was due to the enhanced catalytic activity of Pt/C-3 with a high active surface area.

Initially, all the catalysts were subjected to a continuous potential cycling process (30 cycles), 0.5 M H_2SO_4 at a scan rate of 10 mV s^{-1} to confirm the stability of the samples for further methanol oxidation reaction. This also indicates the strong interaction of Pt NPs with the carbon sample over this potential range. The electro-oxidation of methanol on the Pt supported carbon electrode is carried out in 0.5 M H_2SO_4, which shows a weak hydrogen oxidation/reduction peak. The suppression of the hydrogen adsorption/desorption process leads to the introduction of 1 M CH_3OH to the electrolyte. Based on previous reports,[60] the mechanism[61] of the overall oxidation reaction of CH_3OH molecules is accompanied by the release of electrons through the reaction:

$$CH_3OH + H_2O \rightarrow CO_2 + 6H^+ + 6e^- \quad (7)$$

At potential $E < 0.5$ V, Pt(0) is the initial active site for the C–H bond cleavage in methanol adsorbed on its surface (XPS), and the Pt electrodes in acid media are believed to be involved in the dissociative chemisorption[62] of methanol to give a Pt_3–COH adsorbed species. CH_3OH oxidation on Pt surfaces proceeds *via* a dual path mechanism[63] and the electrons released by the reaction are eventually detected as current by the potentiostat. As the voltage increases, the CH_3OH molecules are dehydrogenated, providing a direct path for oxidation. Pt_3–COH is the reaction intermediate formed during MOR while the PtH species releases H^+ ions into the electrolyte,

$$Pt_3\text{–}COH \rightarrow Pt\text{–}CO + 2Pt + H^+ + e^- \quad (8)$$

It can be seen that over the potential range of 0.3 to 0.9 V the equilibrium formation of OH_{ad} occurs at the surface. Moreover, the naturally anchored nitrogen on the carbon supports[64] provide wettability and water activation to form adsorbed OH_{ad} at a lower potential of 0.3 V which would help to remove the intermediate species formed during MOR. The unreacted Pt_2–CO formed during the reaction rearranges itself to give a linearly bound species which is the poisoning carbonaceous product,

$$Pt_2\text{–}CO \leftrightarrow Pt{=}C{=}O + Pt \quad (9)$$

The CO species produced are the main poisoning species on the Pt surfaces; these compounds impede the CH_3OH oxidation, resulting in a decreased current density. The fact is that the CO_{ad} species acts as a poison when it attaches to Pt while it is resisted from attaching to Pt by the presence of OH_{ad} at all the neighboring sites.[65] On the other hand, H_2O also plays an integral role in the oxidation process, particularly in the removal of adsorbed CO molecules:

$$Pt\text{–}OH_{ad} + H^+ + e^- \rightarrow Pt + H_2O \quad (10)$$

The overall reaction would be,

$$Pt\text{–}OH_{ad} + Pt{=}C{=}O \rightarrow CO_2 + 2Pt + H + e^- \quad (11)$$

The reduced CO_2 may be formed from methanol. The above equation represents the net oxidation reaction of MOR. Typical CVs for the MOR in different potential ranges on Pt/C electrocatalysts in acid media (0.5 M H_2SO_4 + 1 M CH_3OH) are shown in Fig. 8b and the corresponding values of onset potential EP (V), potential at I_f (V), forward peak current I_f (mA), potential at I_b (V), and reverse peak current I_b (mA) for each electrocatalysts were tabulated (Table 3). The first forward sweep was recorded; methanol oxidation starts at 0.33 V and an anodic peak I_f was observed at a higher potential 0.62 V, this current peak (0.32 mA mg^{-1}) can only be due to the faradaic process that occurred during CH_3OH oxidation. Such a high anodic current of Pt/C-3 is commonly thought of as due to the fact that after carbonization almost all the functional groups present in the hydrochar vanish and afford available sites for metal anchoring. This helps the unique interaction between Pt NPs and the high surface area of the carbon support. Pt/C-3 contains OH_{ad} at neighboring sites that could probably eliminate all the strongly absorbed poisonous species (CO, HCOO– and HCO–)[66] and support the MOR. The impact of the higher value of ECSA for Pt/C-3 is in agreement with the MOR activity that physically interprets this as an increased surface area of the Pt catalyst. Also, the increased hydrophilic nature of the hydrochar derived carbon enhances the diffusion of polar reactants such as methanol to the catalytic active sites and provides a clear pathway for the MOR.

The presence of a few functional groups and mild heteroatoms on the edges of the carbon molecules enhances the hydrophilicity and thereby expedites the access of electrolyte to the internal pore structure and increases the effective accessible surface area of the catalyst. Thus, the Pt/C combination provides an open highway network for the easy transport of methanol and the products to and from the catalyst surface. Also, the chemisorption process is less possible beyond 0.6 V as all the steps of reaction (eqn (7)–(11)) appear to occur at the anodic peak potential itself. Furthermore, during the backward sweep, another anodic peak I_b is observed at potential 0.55 V, somewhat less than the I_f potential. Here, the reason for chemisorption and the appearance of the reverse peak is associated with the chemisorption of methanol and the residue of incompletely oxidized carbon species on the surface formed during the forward scan. Therefore, anodic peaks appeared in both forward as well as backward scans. The increase in current rate during the cycling is due to the interaction of Pt particles

Table 3 Calculated M_A and I_f/I_b values of the Pt/C samples

Catalyst	E_P (V)	I_f (V)	I_f (mA cm^{-2})	M_A (A g^{-1})	I_b (V)	I_b (mV cm^{-2})	I_f/I_b
E-TEK	0.34	0.52	0.048	54	0.44	0.025	1.92
Pt/C-1	0.33	0.55	0.006	10	0.65	0.007	0.85
Pt/C-2	0.32	0.60	0.055	45	0.49	0.036	1.52
Pt/C-3	0.31	0.62	0.319	240	0.52	0.200	1.59
Pt/C-4	0.32	0.58	0.11	130	0.48	0.07	1.5

with CO_2, forming Pt–O groups, which gives an increased performance. Methanol tolerance was probed by comparing the I_f/I_b ratios of various electrocatalytic samples; the ratio of the forward oxidation current peak (I_f) to the reverse current peak (I_b) indicates the tolerance of catalysts towards the poisoning species such as adsorbed CO intermediates formed *via* the decomposition of methanol. A higher ratio implies a more effective removal of CO from the catalyst surface.

By comparing the onset potential and anodic current peak of all the catalysts, Pt/C-3 seems to be the best. This situation could be due to the inhomogeneous distribution and agglomerated nature of the Pt nanoparticles on carbon, which is capable of retarding the activity of the electro-oxidation reaction of methanol. During the initial potential scanning, the exact onset potential of Pt/C-3 is observed at 0.31 V (>E-TEK), which indicates that the methanol is readily oxidized and where the hydrogen dissociation occurs, which gives rise to a current peak in the H-region as explained in the dual path mechanism. Also, the reason for such a high current is due to the formation of new active sites emerging from the net hydrogen progression process developed on the platinum surface. This shows that the active sites of the Pt surface were not blocked by strong adsorption species like CO, and the oxidation of methanol was promoted by the reaction intermediates. The exact oxidation of methanol occurred at 0.62 V on the positively directed scan (I_f) with a higher current rate of about 0.31 mA cm^{-2}, and corresponds to the catalytic activity of the functional groups of the carbon surface with a low loading of Pt nanoparticles. Furthermore, Pt/C-3 showed a higher M_A of about 240 A g^{-1}, which may be attributed to the small size and high dispersion of Pt nanoparticles on the carbon and the I_f/I_b ratio is also high compared to the other fabricated catalysts which once again reveals that the electrode fabricated from this catalyst has higher electrocatalytic activity towards MOR. The lower onset potential indicates clearly evidences Pt/C-3 as a superior electrocatalyst for MOR. Thus the increased current density during MOR was due to the enhanced catalytic activity of Pt/C-3 with a high active surface area. There is an increase in the current corresponding to the double layer region, which may be attributed to the electroactive O containing functional groups (which also support the surface activation of carbon materials as confirmed by FT-IR and other studies) at the supporting carbon material, which provide binding sites for anchoring platinum nanoparticles. The decrease in ECSA value indicates that an increasing fraction of Pt surface was being screened due to non-uniform dispersion or increased Pt loading. The increase could be ascribed to the increasing hydrophilicity of the surface-modified CNTs supports, which could enhance the diffusion of polar reactants such as methanol to the catalytic active sites. The higher M_A value of the Pt/C-3 catalyst implies that this would be the best when compared to the other fabricated catalysts as it contributes a higher electrocatalytic activity towards MOR. Moreover, a good efficiency is attained with low catalyst loading.

3.4 Chronoamperometry

Chronoamperometry measurements were made to provide further information on the electrochemical activity, stability and durability of the Pt/C catalyst for methanol oxidation. Fig. 9 shows the current density *vs.* time curves related to the prepared series of Pt/C catalysts. In addition to CV results, it is also important to address the long-term stability of the electrocatalyst for application. In this regard, the stability of all the electrocatalysts was tested by a chronoamperometry technique at the corresponding forward peak potential (0.622 V) for 3500 s in a 0.5 M H_2SO_4 and 1 M CH_3OH solution. The results of Pt/C-1, Pt/C-2 and Pt/C-4 show (Fig. 9a) an initial quasi-equilibrium steady state, which was followed by a slower attenuation upon long time operation and started to decay over longer period of time. This kind of initial sharp decline in the current indicates the poisoning effect of both the metal and the formed intermediate carbonaceous species of CO_{ads}, CH_3OH_{ads} and CHO_{ads} during MOR, and the consumption in the successive scans and surface structural modification of Pt NPs.[67] Moreover, the combined capacitive as well as mass transport effect could be one among the reasons for the initial dwindling-off in current. It can be seen from Fig. 9b that the current density of the Pt/C-3 catalyst rapidly decreases in the initial 100 s due to the initial

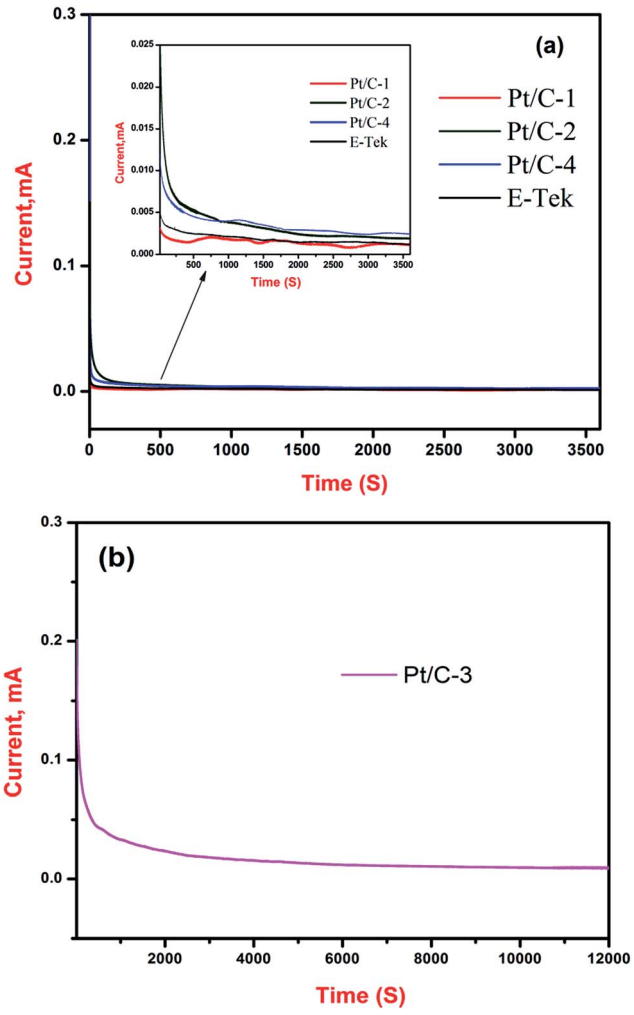

Fig. 9 CA curve of carbonized (a) Pt/C (1–4) catalysts and (b) Pt/C-3 catalyst in 0.5 M H_2SO_4 + 1 M CH_3OH at 700 °C (first point removed).

charging current and the undesirable intermediates are formed during MOR.[68] Then, the drastic suppression slowly occurs at a steady state over a period of more than 10 000 s without showing any bumpy regions along the curve. This situation is consistent with the view that the Pt NPs are homogeneously dispersed and are strongly bound on the surface heteroatoms in the carbon, and therefore accelerated the rate of CO_{ads} oxidation. In particular, the nitrogen groups within the carbon surface strongly repel the Pt, enhancing dispersion and preventing the agglomeration of Pt NPs. Also, the Pt supported functional groups provided the nitrogen in the carbon surface with fewer defects, strengthening the electronic structure, and enhancing the MOR kinetics and stability by a facile removal of CO.[69] The above results clearly demonstrate the Pt/C-3 electrocatalyst displayed an excellent catalytic activity for methanol oxidation and durability due to its favourable morphology, excellent mass activity, functional groups and uniform distribution of Pt NPs compared to the other fabricated electrocatalysts. This pioneering work on the whole exposes how the carbonization temperature and the distribution of platinum on the carbon surface area affects the electro-oxidation of methanol despite similarities in the fabricated samples possessing very similar functionalities, crystal structure, physical texture and elemental composition. An electrocatalyst fabricated with a uniform distribution of Pt NPs having an average particle size of 3–4 nm on a high surface area hydrochar derived carbon, has enhanced electrocatalytic activity towards MOR.

In order to further substantiate the above results, CV and CA analysis were performed for Pt/C-3 electrocatalyst under the same conditions (0.5 M H_2SO_4 and 1 M CH_3OH) with different Pt/C mass loading (10 : 90 and 30 : 70). The results showed well defined chemical adsorption peaks of hydrogen with similar base lines corresponding to the different Pt loadings. These studies have been performed in order to show the Pt loading dependency of Pt/C-3 catalyst during MOR as shown in Fig. 10. Methanol oxidation current peaks for both the catalysts are clearly observed around 0.6 V during the anodic sweep and the cathodic peak is at 0.5 V. This situation shows that the magnitude of the current density is constant at 0.6 V for both the catalysts, which signifies that the MOR depends merely on the Pt surface. Here, the lower loading of Pt on C (10 : 90%) caused a lack of efficiency due to incomplete methanol oxidation and the exaggerated effect of functional groups present on the carbon support whereas overloading Pt on C (30 : 70%) poisons the electrode by the adsorption of CO during MOR.[70] This toxic effect ultimately resulted in shakiness as well as a reduction in current density and cell performance compared to the optimized result shown in Fig. 8. In view of that, a 20 : 80% of Pt/C seems to be the best among the three dissimilar loadings, as this efficiently formed PtO on the surface, which brings about the complete oxidation of methanol. Though, 30 wt% exhibits higher current, the I_f/I_b ratio that denotes the CO tolerance of the catalyst to accumulate carbonaceous species is found to be 2.1 and 1.3 for 10 and 30 wt% of Pt loading on C. A higher value of I_f/I_b attributes to a faster removal rate of the poisoning species arranged on the particle surface and is a good comparison between the electrochemical effectiveness between

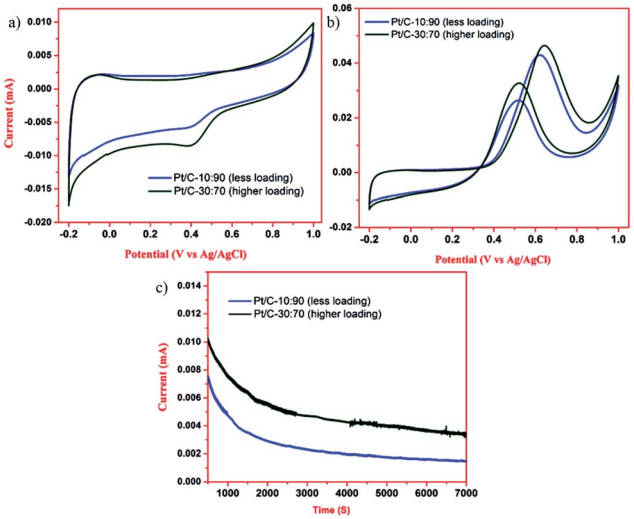

Fig. 10 CV curves of the fabricated Pt/C-3 catalyst with different mass loadings in (a) 0.5 M H_2SO_4, (b) 0.5 M H_2SO_4 + 1 M CH_3OH and (c) CA curve of Pt/C-3 catalyst with different loadings in 0.5 M H_2SO_4 + 1 M CH_3OH.

the prepared catalysts. A chronoamperometry (CA) test for MOR was also carried out at 0.6 V *vs.* Ag/AgCl and the results are shown in Fig. 10c. It can be visibly observed that the currents for both the catalysts dropped rapidly at first and then became moderately stable over time. This is due to the formation of OH_{ads} on Pt, and SO_4^{2-} adsorption on the catalyst surface that decays current by hindering the reaction active sites of platinum decorated carbon for methanol dehydrogenation as time progresses at the particular potential.[70] This fact is the result of a competitive process between CO and methanol adsorption. This outcome reveals that Pt loading is essential in determining the electrocatalytic behaviour of the catalyst and the duration of the treatment. Also, the disability of the functional groups present on the biomass carbon to withstand long periods of time is also a factor in the decay process. The long-term stability and storage property of other Pt/C catalysts will be improved in future.

4. Conclusions

This work blossomed with a high surface area carbon of 431.5 $m^2\ g^{-1}$ sequestered using a natural jackfruit seed powder interwoven with heteroatoms with a mean pore diameter of 3.2 nm and a pore volume of 0.354 $cm^3\ g^{-1}$, which was further homogeneously decorated with Pt NPs *via* a H_2PtCl_6 reduction process. Collectively, four different types of catalysts were prepared *via* HTC with constant temperature, pressure and citric acidic concentration, autoclaved for various reaction times and then thermally carbonized at 700 °C under N_2 stream. Among these four fabricated electrocatalysts, the as synthesized Pt/C-3 is identified as a good catalyst due to its particular features such as surface morphology, texture, functional groups and electrocatalytic activity in the potential range of interest with a high ECSA of 261.4 $m^2\ g^{-1}$. Moreover, the sample Pt/C-3

has a much higher peak current and mass activity of about 0.32 mA mg^{-1} and 54.4 A g^{-1} towards MOR supported by the presence of heteroatoms. In addition, chronoamperometry of Pt/C-3 exposed a very good stability over 6500 s. Furthermore, an experimental investigation of the sample to show the Pt loading dependency of Pt/C-3 once again substantiated that 20 : 80 wt% of Pt/C loading shows a high value of current density with no relevant change in the onset potential and long-time stability during MOR.

Notes and references

1 C. Stone and A. E. Morrison, *Solid State Ionics*, 2002, **152–153**, 1–13.
2 M. Winter and R. J. Brodd, *J. Am. Chem. Soc.*, 2004, **104**, 4245–4269.
3 (*a*) L. Carrette, K. A. Friedrich and U. Stimming, *ChemPhysChem*, 2002, **1**, 162–193; (*b*) K. Kordesch and G. Simander, *Fuel Cells and Their Applications*, VCH, Weinheim, 1996, vol. 1, pp. 1–389.
4 H. Huang and X. Wang, *J. Mater. Chem. A*, 2014, **2**, 6266–6291.
5 A. L. Dicks, *J. Power Sources*, 2006, **156**, 128–141.
6 V. Tulyathana, K. Tananuwonga, P. Songjinda and N. Jaiboonb, *ScienceAsia*, 2002, **28**, 37–41.
7 (*a*) R. Li and A. Shahbazi, *Trends in Renewable Energy*, 2015, **1**, 43–56; (*b*) Z. Liua and R. Balasubramanian, *Procedia Environ. Sci.*, 2012, **16**, 159–166.
8 K. Byrappa and T. Adschiri, *Prog. Cryst. Growth Charact. Mater.*, 2007, **53**, 117–166.
9 A. Chen and P. Holt-Hindle, *J. Am. Chem. Soc.*, 2010, **110**, 3767–3804.
10 H. Liu, C. Song, L. Zhang, J. Zhang, H. Wang and D. P. Wilkinson, *J. Power Sources*, 2006, **155**, 95–110.
11 P. R. Van Rheenen, M. J. Mckelvy and W. S. Glaunsinger, *J. Solid State Chem.*, 1987, **67**, 151–169.
12 H. Ma, X. Z. Xue, J. Liao, C. Liu and W. Xing, *Appl. Surf. Sci.*, 2006, **252**, 8593–8597.
13 N. J. C. Zerega, D. Ragone and T. J. Motley, *Am. J. Bot.*, 2004, **9**, 760–766.
14 K. Rengsutthi and S. Charoenrein, *Food Sci. Technol. Int.*, 2011, **44**, 1309–1313.
15 A. K. Nayak and D. Pal, *Int. J. Biol. Macromol.*, 2013, **62**, 137–145.
16 V. G. Pol, M. Motiei, A. Gedanken, J. C. Moreno and M. Yoshimur, *Carbon*, 2004, **42**, 111–116.
17 B. Hu, K. Wang, L. Wu, S. Yu, M. Antonietti and M. M. Titirici, *Adv. Mater.*, 2010, **22**, 813–828.
18 H. S. Kambo and A. Dutta, *Renewable Sustainable Energy Rev.*, 2015, **45**, 359–378.
19 S. Román, J. M. V. Nabais, C. Laginhas, B. Ledesma and J. F. González, *Fuel Process. Technol.*, 2012, **103**, 78–83.
20 (*a*) Y. Wang, D. L. C. Alsmeyer and R. L. McCreery, *Chem. Mater.*, 1990, **2**, 557–563; (*b*) A. C. Ferrari and J. Robertson, *Phys. Rev. B: Condens. Matter Mater. Phys.*, 2000, **61**, 95–107.
21 J. Zhang, Y. Wang, L. Zhang, R. Zhang, G. Liu and G. Cheng, *Bioresour. Technol.*, 2014, **151**, 402–405.
22 R. J. White, M. Antonietti and M. M. Titirici, *J. Mater. Chem.*, 2009, **19**, 8645–8650.
23 M. M. Titirici, R. J. White, N. Brun and V. L. Budarin, *Chem. Soc. Rev.*, 2015, **44**, 250–290.
24 J. N. Chheda and J. A. Dumesic, *Catal. Today*, 2007, **123**, 59–70.
25 M. M. Titirici and M. Antonietti, *Chem. Soc. Rev.*, 2010, **39**, 103–116.
26 M. Sevilla and A. B. Fuertes, *Chem.–Eur. J.*, 2009, **15**, 4195–4203.
27 S. Kang, J. Ye, Y. Zhanga and J. Chang, *RSC Adv.*, 2013, **3**, 7360–7366.
28 Y. Piao, K. An, J. Kim, T. Yu and T. Hyeon, *J. Mater. Chem.*, 2006, **16**, 2984–2989.
29 W. Oh, J. Kim, H. Kim, M. L. Chen, F. Zhang, K. Zhang and Z. Meng, *J. Korean Ceram. Soc.*, 2009, **46**, 568–573.
30 S. Kang, X. Li, J. Fan and J. Chang, *Ind. Eng. Chem. Res.*, 2012, **51**, 9023–9031.
31 D. Schneider, M. Escala, K. Supawittayayothin and N. Tippayawong, *Int. J. Energy Environ.*, 2011, **2**, 647–652.
32 B. Manoj and A. G. Kunjomana, *Int. J. Electrochem. Sci.*, 2012, **7**, 3127–3134.
33 (*a*) X. Chen, Y. Jiang, J. Sun, C. Jin and Z. Zhang, *J. Power Sources*, 2014, **267**, 212–218; (*b*) C. M. Welch and G. Richard, *Anal. Bioanal. Chem.*, 2006, **384**, 601–619.
34 M. M. Titirici, A. Thomas, S. Yu, O. Muller and M. Antonietti, *Chem. Mater.*, 2007, **19**, 4205–4212.
35 B. Hu, K. Wang, L. Wu, S. Yu, M. Antonietti and M. M. Titirici, *Adv. Mater.*, 2010, **22**, 813–828.
36 B. Hu, S. Yu, K. Wang, L. Liu and X. Xu, *Dalton Trans.*, 2008, **40**, 5414–5423.
37 S. Wena, S. Cui, L. Shi, R. Liang and J. Qiu, *J. Electroanal. Chem.*, 2015, **738**, 77–83.
38 O. V. Sherstyuk, S. N. Pronkin, A. L. Chuvilin, A. N. Salanov, E. R. Savinova, G. A. Tsirlina and O. A. Petrii, *Russ. J. Electrochem.*, 2000, **36**, 741–751.
39 D. Q. Yang, B. Hennequin and E. Sacher, *Chem. Mater.*, 2006, **18**, 5033–5038.
40 L. Zhang, B. Cheng and E. T. Samulski, *Chem. Phys. Lett.*, 2004, **398**, 505–510.
41 C. Bittencourt, M. Hecq, A. Felten, J. J. Pireaux, J. Ghijsen, M. P. Felicissimo, P. Rudolf, W. Drube, X. Ke and G. Van Tendeloo, *Chem. Phys. Lett.*, 2008, **462**, 260–264.
42 C. Dablemont, P. Lang, C. Mangeney, J. Piquemal, V. Petkov, F. Herbst and G. Viau, *Langmuir*, 2008, **24**, 5832–5841.
43 J. Han, G. Xu, B. Ding, J. Pan, H. Dou and D. R. MacFarlane, *J. Mater. Chem. A*, 2014, **2**, 5352–5357.
44 L. Yu, C. Falco, J. Weber, R. J. White, J. Y. Howe and M. M. Titirici, *Langmuir*, 2012, **28**, 12373–12383.
45 P. S. Bagusa, E. S. Ilton and C. J. Nelin, *Surf. Sci. Rep.*, 2013, **68**, 273–304.
46 C. Saka, *J. Anal. Appl. Pyrolysis*, 2012, **95**, 21–24.
47 F. Zhang, H. Ma, J. Chen, G. D. Li, Y. Zhang and J. S. H. Chen, *Bioresour. Technol.*, 2008, **99**, 4803–4808.
48 K. Hammes, R. J. Smernik, J. O. Skjemstad and M. W. I. Schmidt, *Appl. Geochem.*, 2008, **23**, 2113–2122.

49 M. Inaba, M. Ando, A. Hatanaka, A. Nomotob, K. Matsuzawa, A. Tasaka, T. Kinumoto, Y. Iriyama and Z. Ogumid, *Electrochim. Acta*, 2006, **52**, 1632–1638.
50 J. Katesa, S. Junpiromand and C. Tangsathitkulchai, *J. Sci. Technol.*, 2013, **20**, 269–278.
51 T. P. Nevell and S. H. Zeronian, *The Biochar*, E. Horwood Limited, 1985, vol. 7, pp. 1–545.
52 D. B. Jee, A. Jha, K. K. Chattopadhyay, *Microscopy: Science, Technology, Applications and Education*, 2010, vol. 3, pp. 1674–1680.
53 B. Krishnamurthy and S. Deepalochani, *Int. J. Electrochem. Sci.*, 2009, **4**, 386–395.
54 (*a*) A. Walcarius, *Chem. Soc. Rev.*, 2013, **42**, 4098–4140; (*b*) C. Perego and R. Millini, *Chem. Soc. Rev.*, 2013, **42**, 3956–3976.
55 R. N. Singh, R. Awasthi and C. S. Sharma, *Int. J. Electrochem. Sci.*, 2014, **9**, 5607–5639.
56 D. A. Stevens and J. R. Dahn, *J. Electrochem. Soc.*, 2003, **150**, 770–775.
57 E. Brightman, G. Hinds and R. O. Malley, *J. Power Sources*, 2013, **242**, 244–254.
58 A. Pozio, M. De Francesco, A. Cemmi, F. Cardellini and L. Giorgi, *J. Power Sources*, 2002, **105**, 13–19.
59 J. R. Chang, J. F. Lee, S. D. Lin and A. S. Lin, *J. Phys. Chem.*, 1995, **99**, 14798–14804.
60 T. J. Held and F. L. Dryer, *A Comprehensive Mechanism for Methanol Oxidation*, John Wiley & Sons, Inc., 1998, vol. 24, pp. 805–830.
61 S. Park, Y. Xie and M. J. Weaver, *Langmuir*, 2002, **18**, 5792–5798.
62 B. Singh, L. Murad, F. Laffir, C. Dickinsonb and E. Dempsey, *Nanoscale*, 2011, **3**, 3334–3349.
63 E. Herrero, W. Chrzanowski and A. Wieckowski, *J. Phys. Chem.*, 1995, **99**, 10423–10424.
64 W. Fang, *Nanoscale Res Lett.*, 2010, **5**, 68–73.
65 J. Cruickshank and K. Scott, *J. Power Sources*, 1998, **70**, 40–47.
66 Z. Wen, Q. Wang, Q. Zhang and J. Li, *Electrochem. Commun.*, 2007, **9**, 1867–1872.
67 B. Kuppan and P. Selvam, *Prog. Nat. Sci.*, 2012, **22**, 616–623.
68 E. A. Franceschini, M. M. Bruno, F. A. Viva, F. J. Williams, M. Jobbagyc and H. R. Corti, *Electrochim. Acta*, 2012, **71**, 173–180.
69 Z. Yin, M. Chi, Q. Zhu, D. Ma, J. Sune and X. Baof, *J. Mater. Chem. A*, 2013, **1**, 9157–9163.
70 Y. Ma, R. Wang, H. Wang and S. Ji, *Int. J. Electrochem. Sci.*, 2013, **8**, 6085–6093.

